CROSS-COMPARISON OF SELECTED AVALANCHE OBSERVATIONS

Peter Gauer[1,*]

[1]*Norwegian Geotechnical Institute (NGI), Norway*

ABSTRACT: In many mountainous regions, snow avalanches are severe threats to the population and their infrastructure. Delimitation of avalanche endangered areas or the design of sufficient mitigation measures require in-depth understanding on the avalanche phenomenon. Measurements and observation constitute the basis for this understanding. This paper presents a series of avalanche observations or related experiments. From this, some consequences can be deduced that these observations have with regard to avalanche hazards assessment.

Keywords: avalanche observations, full-scale measurements, cross-comparison

1. **INTRODUCTION**

Snow avalanches are severe threats to the population and their infrastructure in many snow covered areas, typically in mountainous regions but also regions that have actually only small relief (< 100 m) (e.g. Issler et al., 2016; Hetu et al., 2011). Delamination of avalanche endangered areas or the design of sufficient mitigation measures require in-depth understanding on the avalanche phenomenon. This understanding bases mostly on observations and measurements of avalanches, but also on small-scale (granular) experiments. Recently, numerical simulations become more and more an additional source of information (e.g. Gaume et al., 2018)—but these models need a thorough validation that relays on avalanche observations, before they can be of use.

2. **METHODS**

NGI has been performing full-scale avalanche experiments and observations at the Ryggfonn test-site (RGF) in Western Norway for more than 40 years (Gauer and Kristensen, 2016). The acquired data constitute the basis for the presented cross-comparison with data originating from various other sites around the world, for example, Vallée de la Sionne (VDLS) (Ammann, 1999) or Col du Lauteret (CDL) (Eybert-Berard et al., 1978).

The RGF-site is locate in Western Norway, in the community of Stryn (61.96° N, 7.275° E). The usual release area is located in a north facing cirque at an elevation of about 1600 m asl. The track is slightly channelized and has a total drop of about 950 m and a mean slope angle of around 30°. Fig. 1 shows a map of the area and Fig. 2 parts of the original instrumentation including a powerline assembly.

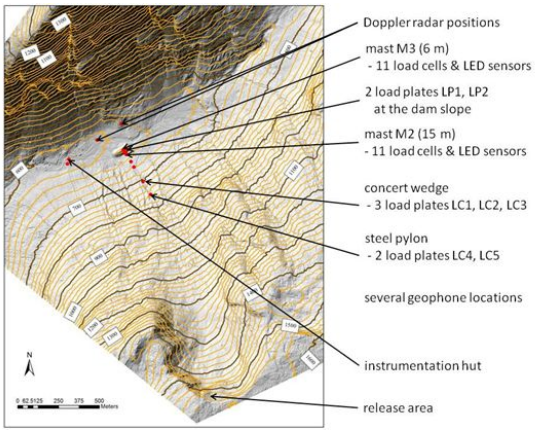


Figure 1: Map of the Ryggfonn (RGF) test-site.

Further information on the RGF-site can be found in (Gauer et al., 2010a) as well as in (Barbolini and Issler, 2006), which provides also information about the other test-sites like VDLS or CDL.



Figure 2: Concrete wedge with load plates LC321 (0.6 m × 1.2 m each) and transmission line build in 1982 with the gridder mast carrying the tension sensors SC654. In the right background the 16 m high catching dam. (Photo NGI)

*Corresponding author address:
Peter Gauer, Norwegian Geotechnical Institute,
P.O. Box 3930 Ullevaal Stadion, NO–0806 Oslo, Norway
Tel: ++47 45 27 47 43; Fax: ++47 22 23 04 48; E-mail: pg@ngi.no

3. OBSERVATIONS

3.1. Velocity measurements

Avalanche velocity is an important dynamics factor. The velocity determines largely the path an avalanche descent and it strongly influences the runout distance, especially for dry-mixed avalanches. The velocity is decisive for the dimensioning of mitigation measures like catching dams (cf. Jóhannesson et al., 2009). Therefore, it is inevitable for practitioners in the field to have an idea about velocities that need to be expected in a given path.

Most observations, which are available, originate from few test-sites. That limits the meaningfulness in respect to the influence of varying terrain parameters, such as slope steepness and total drop height. Fig. 3 shows a collection of velocity observations from various experiments and avalanche paths. To enable comparison with other tracks, the geometry is scaled by the total drop height H_{SC} and the velocity by $\sqrt{gH_{SC}/2}$. Fig. 3 a shows a set of granular small scale tests (Hutter and Koch, 1991) with varying initial slope angles and granular material. These tests were part for the model validation of the so-called Savage-Hutter model (Savage and Hutter, 1991). Panel b shows velocity measurements from ping pong ball experiments on a ski jump by (Ogura et al., 2003; McElwaine and Nishimura, 2001). In contrast to many other granular small scale test, which involve “infinite” long chutes with constant slopes, the previous experiments were done on parabolic-like tracks and hence closer to real avalanche tracks. Fig. 3 c shows a summary of measurements of the front velocity along the entire track as well as observations between specific points at RGF. It presents the measured mean front velocity and the corresponding $\pm\sigma$-range. In addition the upper envelope of the maximum velocity observed is given. Fig. 3 d presents a compilation of measurements from “major” dry-mixed avalanches in various paths around the world (cf. Gauer, 2014, 2013, and references therein). Here and in the following, the term “major events” is used in the sense that these avalanches have return periods of at least several years and can be considered large relative to the path, but not necessary the most extreme. That means they can be classified as R4 or R5 (cf. Greene et al., 2016, 3.6.5.2 Size - relative to path). The total drop height in these cases ranged from about 120 m to 1220 m. The velocities may represent the upper range of the expected avalanche velocities along a path. This is in agreement with the observations from RGF, from where the highest observed velocities fit well into the shown observations. A further comparison of observed maximum velocities can be found in (e.g. McClung and Gauer, 2018).

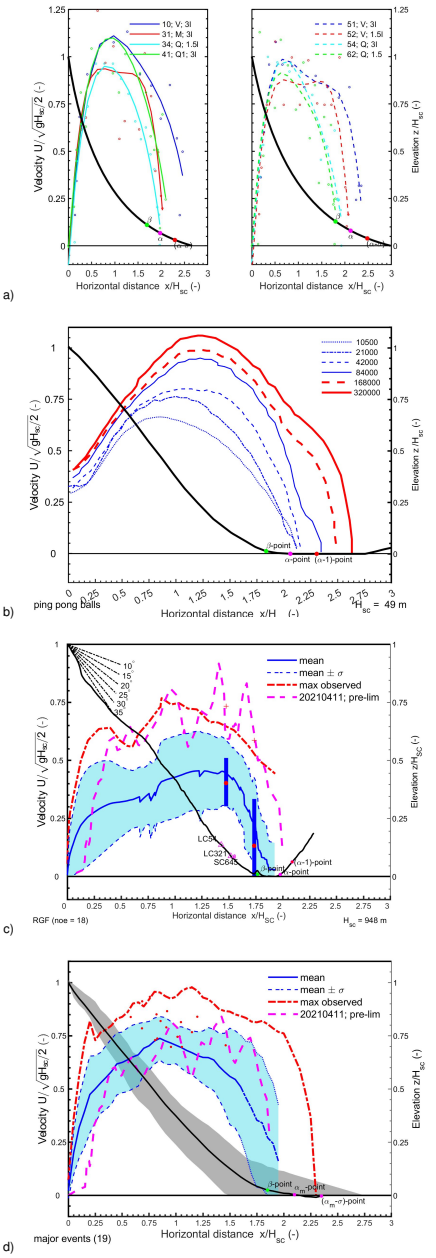


Figure 3: Range of front velocities along the track: a) Granular chute experiments by Hutter and Koch (1991); b) Ping pong ball experiments on a ski jump by Ogura et al. (2003). The different lines show experiments with different numbers of ping pong balls. c) measurements at the RGF-site. The blue line shows the mean, the shaded area the $\pm\sigma$-range and the red dashed-dotted line the observed maximum until 2021 derived from observations along the track. The red dashed line shows the recent event from 2021-04-11. In addition, bars show the interquartile range of the front velocity U_{LC} measured between load plates LC54 and LC321 and the front velocity U_b at the base of the catching dam, the red dots show the corresponding means and red crosses mark the measured maxima. d) Compilation of measurements from various (major) avalanches. The red dots mark the maximum of the different measurements. The black line represents a “mean path” geometry and the gray shaded area the envelope of all path geometries. As a reference, the β-, α-, and (α-σ)-point are shown in all panels (for explanation see Lied and Bakkehøi, 1980).

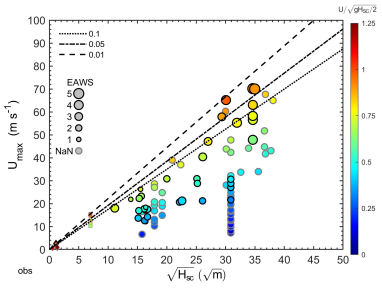


Figure 4: Collection of observed maximum velocities versus the square root of the drop height $\sqrt{H_{SC}}$. The color illustrates the scaled velocity $U_{SC} = U_{max}/\sqrt{gH_{SC}/2}$ and the marker size corresponds to the EAWS avalanche size classes, if known. The ♦ (bottom left) show the granular experiments and the ■ the ping pong ball experiments in Fig. 3. The lines show the estimated exceedance probabilities derived from observations.

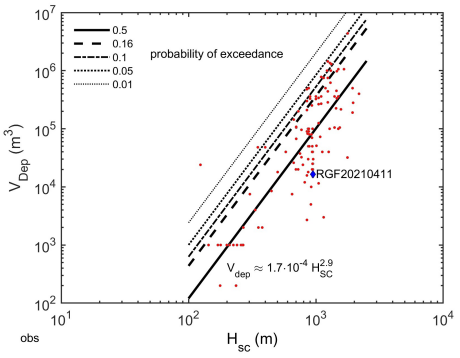


Figure 5: Observed avalanche deposits of "major events" versus total drop height H_{SC} (for references to the data see Gauer et al., 2010b). the ⋄ indicates the volume of the 2021-04-11 event at the Ryggfonn test site. The lines show the estimated exceedance probabilities derived from these observations.

Although on the first glance the granular and the ping pong ball experiments seem to be barely related to snow avalanches, the velocity measurements show surprising similarities. For the "major events" (panel d), the observations suggests that the maximum front velocity is proportional to the square root of the fall height, that is

$$U_{max} \sim \sqrt{gH_{SC}/2}\,. \qquad (1)$$

McClung and Schaerer (2006) proposed a similar relation as a kind of upper limit based on observations from Rogers Pass, Canada. Although, some reports indicate that highly fluidized avalanches may have reached higher maximum velocities (Gauer, 2014, and references therein). The scaling of the upper envelope can also be seen Fig. 4, which shows a collection of observed maximum velocities along various avalanche tracks, among them a series of observations from Ryggfonn.

As all dynamical avalanche models solve the (depth averaged) momentum or velocity equation(s), respectively, velocity measurements along the path and/or at selected locations are most import for validating those models. Therefore, the scaling behavior of the velocity can give some insight into the performance of numerical models such as the Voellmy-model (Voellmy, 1955, 1964), the PCM-model (Perla et al., 1980), and more advanced ones, like RAMMS (Christen et al., 2010), SAMOS-AT (Sampl and Granig, 2009) or similar ones. Examples of a performance test can be found in (Gauer, 2023, same proceeedings).

3.2. Avalanche size

Fig. 5 shows observed avalanche deposit volumes of "major avalanche events" versus their total drop height H_{SC}. Obviously, there is a trend for larger avalanches from larger drop heights. Part of this tendency can probably accounted for by snow entrainment along the track and not solely by the release size. Avalanche mass or volume is often taken as indicator for the destructive potential (c.f. the CASC in McClung and Schaerer, 2006), and the estimated size also often determines the parameter choice in the avalanche models in the way that larger release volumes favor faster avalanches and longer runtouts (c.f. Bartelt et al., 2017). McElwaine and Nishimura (2001) propose that the velocities in their ping pong ball experiments follow $u \propto N_{oP}$, where N_{oP} is the number of balls. However, size is not the only thing what matters. This can, for example, be seen in the 2021-04-11 event at Ryggfonn, which was rather small in size, but it is the fastest observed one until now with a rather long runout (see Figs. 3 and 4). The question then arises whether the absolute initial size is a good indicator for the choice of model parameters.

3.3. Avalanche frontal structure

Fig. 6 a shows a principal sketch of a dry-mixed avalanche as it is believed a present (Gauer et al., 2008a; Sovilla et al., 2015). However, few measurements that could help to quantify the picture exist. McElwaine (2005) was looking into the structure of gravity currents and he confirmed that the angle of the front to the slope should be about 60°. Fig. 6 b shows the arrival time of the front of an avalanche at the two masts M2 in front and M3 on top of the dam at the Ryggfonn test site (c.f. Fig. 1). The time delay between the various heights can give some indication of the frontal slope. The avalanche velocity at M2 was approximately 28 m s^{-1} and the time delay between top and bottom sensors 0.4 s. The effective height difference between the sensor pairs catching the frontal slope was about 12.5 m. With this the frontal slope can be estimate to approximately 50°.

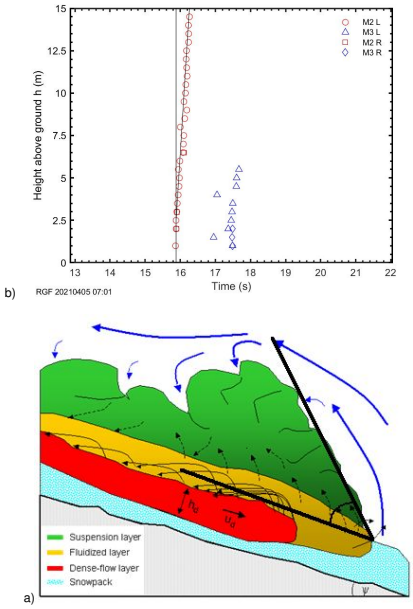


Figure 6: a) Schematic figure of a dry-snow avalanche showing the dense core, the fluidized (saltation) layer and the powder cloud (c.f. Gauer et al., 2008a). b) Arrival time of the front of avalanche 20210405 at mast M2 and M3 at various heights above ground.

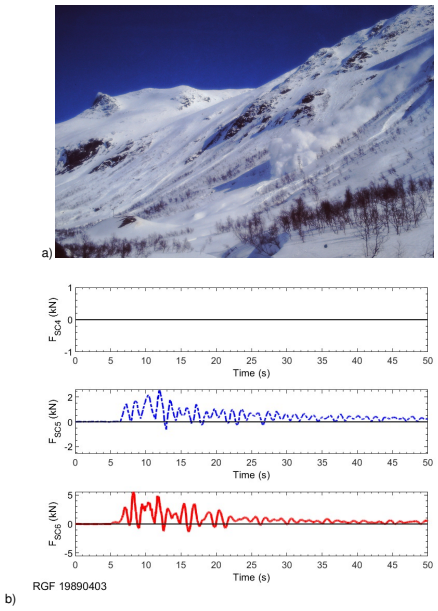


Figure 7: The avalanche 19890403 just arriving at the powerline assembly at the Ryggfonn test site (panel a; photo K. Kristensen/NGI). Tension measurements (panel b; data are reproduced from plots); unfortunately no data from the uppermost line are available for this event. The first eigenfrequency of the transmission line was about $f_1 = 0.1$ Hz.

3.4. Forces on transmission line cables

There exist almost no measurements of avalanche parameters above the dense/fluidized layer of an avalanche (i.e. for heights higher than 4 to 6 m above ground). In the early years of the RGF site, a transmission line assembly was mounted in the lower part of the track (see Fig. 2) with three cables at heights of about 8 m, 12 m, and 16 m above ground. The location of the assembly is indicated in Fig. 3 b) with SC645.

A limited set of data was obtained during the period 1983 to 1989, which provides some idea about the probable pressure distributions with height. Generally, the avalanche caused sinusoidal tension forces (i.e. the cable started a damped swinging with a frequency in the range of 0.3 Hz to 1 Hz), where the maximum tension forces could be observed early during the avalanche passage.

The conversion of the measured tension forces to the avalanche impact pressure on the cables is not straight forward as it depends on the impact location and the width of the impacted area on the cable. The effective width of the impacted area is rather uncertain. Furthermore, the resulting force on the cable is depending on the avalanche pressure and the own weight of the cables and therefore is not necessarily collinear with the flow direction of the avalanche. In the setting from Ryggfonn an amplification by a factor in the range of 5 to 10 might be reasonable (The original static tests on the cable suggested a factor 6.4.) Nonetheless, some rough estimations are possible by some sag tension calculations (see e.g. Task Force B2.12.3, 2016). Fig. 8 a shows a boxplot of the estimated pressure ranges at the three heights within the suspension layer. The quantitative values involve some uncertainties, however, qualitatively the decrease with height above ground seems reasonable. The values are corrected in respect to the estimated snow on the ground and estimated flow height of the dense/fluidized part.

The observed pressures can be approximated by

$$P(z_{ai}) = C_D \rho_{ai} \frac{U_f^2}{2} \exp(-e_c\, z_{ai}) \,, \qquad (2)$$

where e_c has the unit m^{-1} and depends on the velocity as

$$e_c \approx \max(0.583 - 0.0088 U_f, 0.05) \,. \qquad (3)$$

Here, U_f is the front velocity, z_{ai} is the vertical height above the interface between dense/fluidized layer and the powder part, ρ_{ai} is a representative avalanche density at this interface and C_D the drag factor for a power line ($C_D \sim 1$). Fig. 8 b shows estimates on the normalized pressure profiles based on the measurements for various velocities. The height of the profile is given by the point where the normal wind pressure with the same wind velocity causes the same tension force in the cable. The back calculations suggest that the interquartile range of effective density ρ_{ai} at the interface was [7.4, 18.2] kg m^{-3} with a median of around 12.4 kg m^{-3} and a mean of

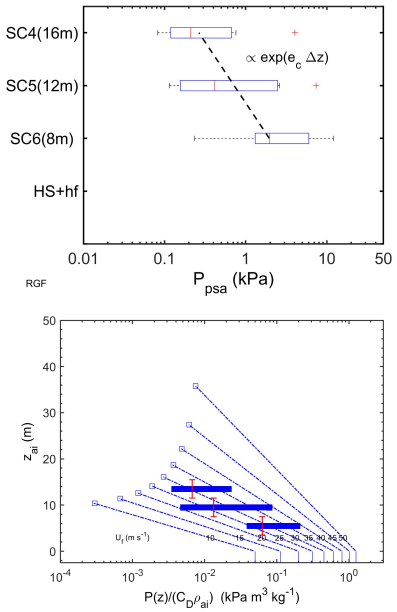


Figure 8: a) Boxplot of the estimated pressure distribution within the suspension layer based on the observations at transmission lines at 3 heights above ground. The median is shown by the red central mark, the 25th–75th percentile as edges of the blue box, the whiskers extend to the most extreme data points not considered outliers and outliers are marked with a red cross. The height HS+hf indicates the estimated interface between dense/fluidized layer and the powder part. b) Estimates on the normalized pressure profile $P(z_{ai})/(\rho_{ai}\, C_D)$ based on measurements at the RGF-site. The bars show the interquartile range of the measurements where the vertical lines indicate the median and the uncertainty range of the height. The dash-dotted lines show predictions according Eq. (2) with the front velocity U_f as parameter. The squares indicate the upper boundary of the powder part where the density has diminished and is close to the density of air. Note the log-scale of the x-axis.

around 16 kg m^{-3}. As mentioned, these values are hampered by considerable uncertainty and should only be seen as order of magnitude.

3.5. Impact pressure on mast like obstacles

The design of masts for electrical power lines, ski lifts, or cable cars in avalanche prone terrain requires knowledge about (impact) forces of snow avalanches on narrow obstacles. Recent observations show that avalanches, especially wet-snow ones, can cause large forces on this kind of obstacles (Gauer et al., 2008b; Sovilla et al., 2010; Thibert et al., 2013; Ancey and Bain, 2015). Following the ansatz proposed in (Jóhannesson et al., 2009, Eq. (12.6)), the force on an obstacle might be expressed by

$$F_D \approx \rho C_D^* \left(1 + \frac{f_{CD}}{\mathbf{Fr}^2}\right) A \frac{U^2}{2} \qquad (4)$$

where **Fr** is the Froude number (= $U/\sqrt{g\,h}$), U the velocity, h the flow height, A the projected area, and

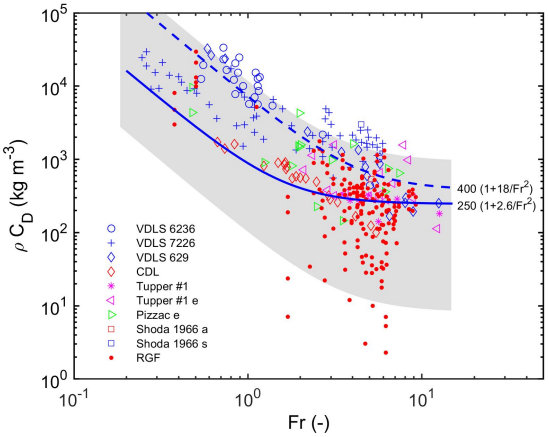


Figure 9: Estimates on the effective $\rho\, C_D$ vs. **Fr** (= $U/\sqrt{g\,h}$) based on measurements at various avalanche test-sites. The continuous line shows an upper limit (0.9 quantile) from measurements with load plates at RGF (location LC54 and LC321 in Fig. 3 b) for dry-snow events; the dashed line shows a corresponding limit for wet-snow events. The gray shaded area indicates the quantile range between 0.1 and 0.9 for all measurements combined.

ρ is the avalanche density. The coefficients C_D^* describes the effect due to the dynamic pressure and f_{CD} the additional contribution by static pressure. Both coefficients may depend on the flow properties themselves and on the geometry of the obstacle and snow clods involved. Fig. 9 shows estimates on the combination of flow density and effective drag factor C_D based on observed impact pressures from various test sites. The velocity and flow height measurements / estimates may involve considerable uncertainties and therefore, the Froude numbers here should only be regarded as an indication of the flow state. However, the data give a consistent impression. The dashed line may give an approximation for the upper envelope for measurements of wet-snow avalanches and the continuous one for dry-snow avalanches at the RGF-site.

3.6. Effect of a catching dam

The avalanche catching dam, which can be seen in the background of Fig. 2, makes the RGF-site unique. It allows to study the efficiency of this kind of an avalanche mitigation measure at full-scale. Fig. 10 shows a series of observations from RGF for which velocity and measurements of the runout distance are available. The data suggest that the effect of the dam is limited and diminishes especially for dry snow avalanches above a certain velocity. This is also reflected in Fig. 11, which shows a comparison of the probability of exceedance between the observations and Monte-Carlo simulations. To this end, a simple mass block model was used on a terrain profile with and without dam included. The probability distributions for the velocity and the retarding acceleration were derived from the measure-

ments (for more details see Gauer et al., 2009). The simulations imply that the probability of exceedance is only effected in an area close to the dam itself. The dam has little or no effect on faster avalanches. The simulations with dam are in accordance with the observations.

Fig. 12 shows a plot of the simulated joint probability distribution of the runout distance versus the velocity at the hillside base of the dam. For comparison, the overrun length is scaled by the design height of the dam, H_D, und the velocity scaled by $\sqrt{2\,g\,H_D}$. The overrun length of observed avalanches that surpassed the dam crown can be estimated by

$$\frac{l_{ovr}}{H_{fb}} = b_1 \frac{U_b^2}{2gH_{fb}} + b_0\,, \qquad (5)$$

where H_{fb} is the effective free board of the dam ($H_{fb} \le H_D$), U_b is the front velocity at the upstream of the base of the dam. $b_1 \approx 2.56$ and $b_0 \approx -1.41$, respectively.

Similar relations were also obtained in granular small-scale experiments (for references see Gauer and Kristensen, 2005; Faug et al., 2008). Fig. 13 shows a comparison between the observations at RGF and small-scale granular experiments. Although all experiments show a qualitative similarity, there are distinct quantitative differences between the full-scale avalanche experiments and the small-scale granular ones. For example, the normalized kinetic energy in the granular is considerably higher than in the full scale tests. There are also considerable differences between the granular experiments.

Eq. 6 suggests that the maximum vertical run-up H_r can be estimated by

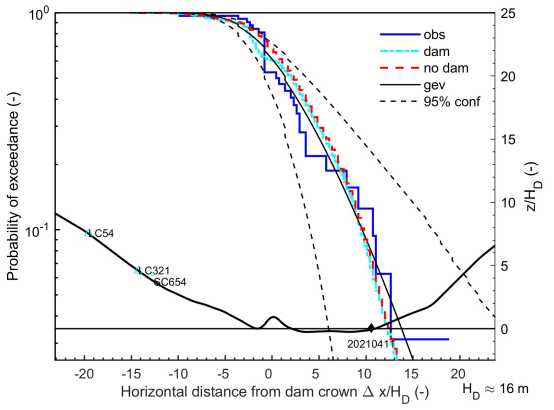


Figure 11: Survival function of the observed runout (obs until 2008) at RGF. The ♦ shows the avalanche event 20210411. The line marked with "gev" plots a fit according to a generalized extreme value distribution and the corresponding 95% confidential interval is marked by "95% conf". Monte-Carlo simulations with and without dam are included. The path profile in the runout area is shown, where the topography is scaled by the design height of the dam $H_D \approx 16$ m, which is approximately 1.6% of the total drop height H_{SC} at RGF. The locations of the load plates LC54 and LC321 are marked by △ and the location of the former powerline assembly SC654 by ○.

$$\frac{H_r}{(U_b^2/2g)} \approx c_1\,, \qquad (6)$$

where the constant c_1 might be in the order 1 according to Fig. 13. This is in complete agreement with other avalanche observations (e.g. Jóhannesson et al., 2009, Fig. 5.12). The granular experiments by Chu et al. (1995), on the hand, would suggest c_1 in the order of 0.1, which could imply a much higher efficiency of a catching dam. In their theoretical considerations Chu et al. (1995) come up with c_1-values of a round 0.6, which is still lesser than the observations show for major

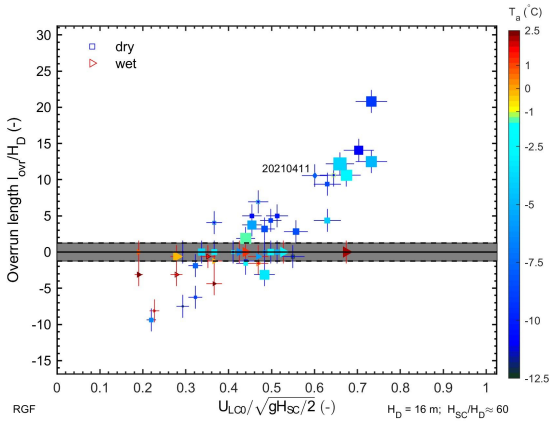


Figure 10: Overrun length l_{ovr} versus velocity U_{LC} at the entrance of the runout area half ways between the locations of LC54 and LC321. The length is scaled by the design heigth of the dam $H_D = 16$ m and the velocity is normalized by $\sqrt{gH_{SC}/2}$. The avalanche were classified either as wet or dry. The colors show the air temperature at the day of the event. The gray shaded area indicate the width of the dam.

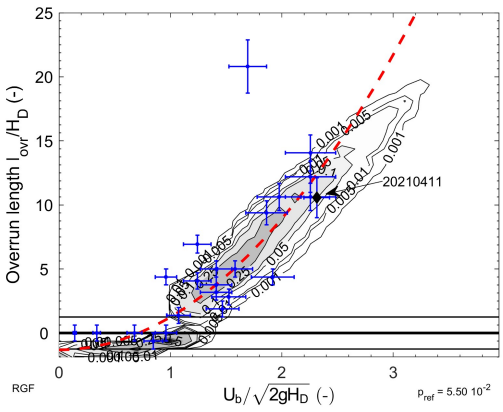


Figure 12: Joint probability distribution of the normalized runout distance l_{ovr}/H_D versus the normalized velocity $U_b/\sqrt{2gH_D}$. For the observation, h_{fb} is used instead H_D. Probability is normalized by $p_{ref} = 5.5 \cdot 10^{-2}$. Errorbars indicate the measurements and the dashed line shows the fit according to Eq. (6). The ♦ shows the avalanche event 20210411, which fit very well into the prediction.

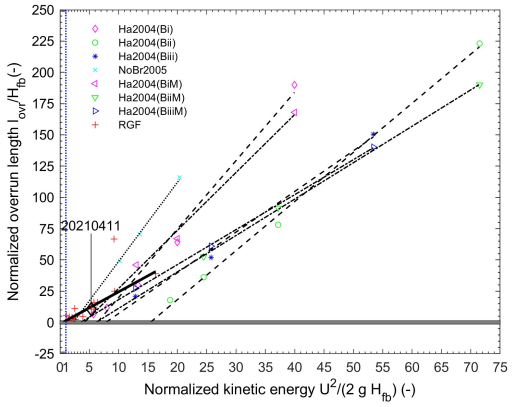


Figure 13: Correlation between normalized kinetic energy and normalized overrun length; H_{fb} is the effective free board at the time of the event (for the granular expriments see Hákonardóttir, 2004; Norem and Brateng, 2005). The ◊ marks the avalanche event 20210411.

avalanches.

4. CONCLUDING REMARKS

NGI has been performing full-scale avalanche experiments and observations at the Ryggfonn test-site in western Norway for more than 40 years (Gauer and Kristensen, 2016). The acquired data constitute the basis for the presented cross-comparison with data originating from various other sites around the world, for example Vallée de la Sionne (Ammann, 1999) or Col du Lauteret (Eybert-Berard et al., 1978) and with small-scale granular-experiments (e.g. Ogura et al., 2003; Hákonardóttir, 2004; Norem and Brateng, 2005).

These avalanche experiments provide valuable data. The measurements give, for example, directly indications on expected forces or on the efficiency of mitigation measures, like catching dams. However, to obtain in-depth understanding in avalanche dynamics, cross-comparisons between different avalanche paths or test-sites are necessary to uncover, e.g., possible scaling relations. Full-scale avalanche tests are time consuming—only a limited number of experiments are possible per year—and they are expensive. Therefore, small-scale granular as well as snow chute experiments seem to be appealing. However, in order to draw sustainable results from these, a cross-comparison with large scale experiments is needed. The same holds true for results of numerical models. For a discussion on this topic see the accompanying paper Gauer (2023).

ACKNOWLEDGMENTS

Parts of this research was financially supported by the Norwegian Ministry of Oil and Energy through the project grant “R&D Snow avalanches 2017 - 2019” to NGI, administrated by the Norwegian Water Resources and Energy Directorate (NVE).

REFERENCES

Ammann, W. J. (1999). A new Swiss test-site for avalanche experiments in the Vallée de la Sionne/Valais. *Cold Regions Science and Technology*, 30(1–3):2–11.

Ancey, C. and Bain, V. (2015). Dynamics of glide avalanches and snow gliding. *Reviews of Geophysics*, 53:745–784.

Barbolini, M. and Issler, D. (2006). Avalanche Test Sites and Research Equipment in Europe: An Updated Overview. Final-Report Deliverable D8, SATSIE Avalanche Studies and Model Validation in Europe.

Bartelt, P., Bühler, Y., Christen, M., Deubelbeiss, Y., Salz, M., Schneider, M., and Schumacher, L. (2017). *RAMMS User Manual v.1.7.0 Avalanche*. WSL Institute for Snow and Avalanche Research SLF.

Christen, M., Kowalski, J., and Bartelt, P. (2010). RAMMS: Numerical simulation of dense snow avalanches in three-dimensional terrain. *Cold Regions Science and Technology*, 63:1–14.

Chu, T., Hill, G., McClung, D. M., Ngun, R., and Sherkat, R. (1995). Experiments on granular flows to predict avalanche runup. *Canadian Geotechnical Journal*, 32(2):285–295.

Eybert-Berard, A., Perroud, P., Brugnot, A. Mura, R., and Rey, L. (1978). Mesures dynamiques dans l’avalanche — résultats expérimentaux du Col du Lautaret (1972-1978). In ANENA, editor, *Proceedings of the Second International Meeting on Snow and Avalanches, 12–14 April 1978, Grenoble, France*, 2nde Rencontre Internationale sur la Neige et les Avalanches Societé Hydrotechnique de France, Grenoble, pages 203–224, ANENA, Grenoble, France.

Faug, T., Gauer, P., Lied, K., and Naaim, M. (2008). Overrun length of avalanches overtopping catching dams: Cross-comparison of small-scale laboratory experiments and observations from full-scale avalanches. *Journal of Geophysical Research: Earth Surface*, 113:F03009(1–17).

Gauer, P. (2013). Comparison of avalanche front velocity measurements: supplementary energy considerations. *Cold Regions Science and Technology*, 96:17–22.

Gauer, P. (2014). Comparison of avalanche front velocity measurements and implications for avalanche models. *Cold Regions Science and Technology*, 97:132–150.

Gauer, P. (2023). What avalanche observations tell us about the performance of numerical models. In *Proceedings of the International Snow Science Workshop 2023, Bend, OR*.

Gauer, P., Breien, H., Issler, D., Kristensen, K., Kronholm, K., Lied, E., and Lied, K. (2010a). The upgraded full-scale avalanche test-site Ryggfonn, Norway. In *Proceedings of the International Snow Science Workshop, Lake Tahoe, CA, October, 17–22, 2010*, pages 747–752.

Gauer, P., Issler, D., Lied, K., Kristensen, K., and Sandersen, F. (2008a). On snow avalanche flow regimes: Inferences from observations and measurements. In *Proceedings of the International Snow Science Workshop 2008, September 21- 27, Whistler, British Columbia, Canada*, pages 717–723.

Gauer, P. and Kristensen, K. (2005). Avalanche Studies and Model Validation in Europe, SATSIE; Ryggfonn measurements: Overview and dam interaction. NGI Report 20021048-10, Norwegian Geotechnical Institute, Sognsveien 72, N-0806 Oslo.

Gauer, P. and Kristensen, K. (2016). Four decades of observations from NGI’s full-scale avalanche test site Ryggfonn—summary of experimental results. *Cold Regions Science and Technology*, 125:162–176.

Gauer, P., Kronholm, K., Lied, K., Kristensen, K., and Bakkehøi, S. (2010b). Can we learn more from the data underlying the statistical α-β model with respect to the dynamical behavior of avalanches? *Cold Regions Science and Technology*, 62:42–54.

Gauer, P., Lied, K., and Kristensen, K. (2008b). On avalanche measurements at the Norwegian full-scale test-site Ryggfonn. *Cold Regions Science and Technology*, 51:138–155.

Gauer, P., Lied, K., and Kristensen, K. (2009). Analysis of avalanche measurements out of the runout area of NGI's full-scale test-site Ryggfonn. *Cold Regions Science and Technology*, 57(1):1–6.

Gaume, J., Gast, T. F., Teran, J., van Herwijnen, A., and Jiang, C. (2018). Unified modeling of the release and flow of snow avalanches using the material point method. In *Proceedings of the International Snow Science Workshop 2018, Innsbruck, Austria*.

Greene, E., Atkins, D., Birkeland, K., Elder, K., Landry, C., Lazar, B., McCammon, I., Moore, M., Sharaf, D. Sternenz, C., Tremper, B., and Williams, K. (2016). Snow, weather, and avalanches: Observation guidelines for avalanche programs in the united states. Technical report, American Avalanche Association.

Hákonardóttir, K. M. (2004). *The Interaction Between Snow Avalanches and Dams*. Phd thesis, University of Bristol , School of Mathematics, University of Bristol.

Hetu, B., Brown, K., and Germain, D. (2011). Fatal avalanche accidents in Quebec (Canada) 1825 to 2009. *Canadian Geographer-Geographe Canadien*, 56:273–287.

Hutter, K. and Koch, T. (1991). Motion of a granular avalanche in an exponentially curved chute: experiments and theoretical predictions. *Proceedings of the Royal Society of London. Series A: Mathematical, Physical and Engineering Sciences*, 334(1633):93–138.

Issler, D., Jonson, A., Gauer, P., and Domaas, U. (2016). Vulnerability of houses and persons under avalanche impact - the avalanche at Longyearbyen on 2015-12-19. In *Proceedings of the International Snow Science Workshop 2016, Breckenrigde, CO.*

Jóhannesson, T., Gauer, P., Issler, D., and Lied, K., editors (2009). *The design of avalanche protection dams. Recent practical and theoretical developments*. Number EUR 23339 in Climate Change and Natural Hazard Research Series 2. European Commission, Directorate-General for Research. ISBN 978-92-79-08885-8, ISSN 1018-5593.

Lied, K. and Bakkehøi, S. (1980). Empirical calculations of snow-avalanche run-out distance based on topographic parameters. *Journal of Glaciology*, 26(94):165–177.

McClung, D. and Schaerer, P. (2006). *The Avalanche Handbook*. The Mountaineers Books, 1011 SW Klickitat Way, Seattle, Washington 98134, 3rd edition.

McClung, D. M. and Gauer, P. (2018). Maximum frontal speeds, alpha angles and deposit volumes of flowing snow avalanches. *Cold Regions Science and Technology*, 153:78–85.

McElwaine, J. (2005). Rotational flow in gravity current heads. *Philosophical Transactions of the Royal Society A-Mathematical Physical and Engineering Sciences*, 363:1603–1623.

McElwaine, J. and Nishimura, K. (2001). Ping-pong ball avalanche experiments. *Annals of Glaciology*, 32(1):241–250.

Norem, H. and Brateng, L. E. (2005). Effect of dams and mounds to retain snow avalanches. In K., K. S., Flaate, K., and Larsen, J., editors, *Landslides and Avalanches: ICFL 2005, Norway*, pages 279–285, London, U. K. Taylor & Francis Group.

Ogura, T., Mcelwaine, J., and Nishimura, K. (2003). Drag forces and ping-pong ball avalanches [in japanese]. *Journal of the Japanese Society of Snow and Ice*, 65(2):117–125.

Perla, R., Cheng, T. T., and McClung, D. M. (1980). A two-parameter model of snow-avalanche motion. *Journal of Glaciology*, 26(94):119–207.

Sampl, P. and Granig, M. (2009). Avalanche simulation with SAMOS-AT. In *Proceedings of the International Snow Science Workshop, Davos*, pages 519–523.

Savage, S. and Hutter, K. (1991). The dynamics of avalanches of granular materials from initiation to runout. Part I: Analysis. *Acta Mechanica*, 86(1-4):201–223.

Sovilla, B., Kern, M., and Schaer, M. (2010). Slow drag in wet snow avalanche flow. *Journal of Glaciology*, 56(198):587–592.

Sovilla, B., McElwaine, J., and Louge, M. Y. (2015). The structure of powder snow avalanches. *Comptes Rendus Physique*, 16:97–104.

Task Force B2.12.3 (2016). Sag-tension calculation methods for overhead lines. Technical report.

Thibert, E., Faug, T., Bellot, H., and Baroudi, D. (2013). Avalanche impact pressure on a plate-like obstacle. In *International Snow Science Workshop Grenoble, Chamonix, Mont-Blanc, 2013*, pages 663–670.

Voellmy, A. (1955). Über die Zerstörungskraft von Lawinen. *Schweizerische Bauzeitung*, Sonderdruck aus dem 73. Jahrgang(12, 15, 17, 19 und 37):1–25.

Voellmy, A. (1964). On the destructive force of avalanches (translation by R. E. Tate). Translation 2, Alta Avalanche Study Center Wasatch National Forest. translate by R. E. Tata.